Detection of solar wind-produced water in irradiated rims on silicate minerals

John P. Bradley[a,b,1], Hope A. Ishii[a,b], Jeffrey J. Gillis-Davis[b], James Ciston[c], Michael H. Nielsen[d,e], Hans A. Bechtel[f], and Michael C. Martin[f]

[a]Institute of Geophysics and Planetary Physics, Lawrence Livermore National Laboratory, Livermore, CA 94550; [b]Hawaii Institute of Geophysics and Planetology, University of Hawaii at Manoa, Honolulu, HI 96822; [c]National Center for Electron Microscopy, [d]Materials Science Division, and [f]Advanced Light Source Division, Lawrence Berkeley National Laboratory, Berkeley, CA 94720; and [e]Department of Materials Science and Engineering, University of California, Berkeley, CA 94720

Edited by Mark H. Thiemens, University of California at San Diego, La Jolla, CA, and approved December 23, 2013 (received for review October 25, 2013)

The solar wind (SW), composed of predominantly ~1-keV H^+ ions, produces amorphous rims up to ~150 nm thick on the surfaces of minerals exposed in space. Silicates with amorphous rims are observed on interplanetary dust particles and on lunar and asteroid soil regolith grains. Implanted H^+ may react with oxygen in the minerals to form trace amounts of hydroxyl (−OH) and/or water (H_2O). Previous studies have detected hydroxyl in lunar soils, but its chemical state, physical location in the soils, and source(s) are debated. If −OH or H_2O is generated in rims on silicate grains, there are important implications for the origins of water in the solar system and other astrophysical environments. By exploiting the high spatial resolution of transmission electron microscopy and valence electron energy-loss spectroscopy, we detect water sealed in vesicles within amorphous rims produced by SW irradiation of silicate mineral grains on the exterior surfaces of interplanetary dust particles. Our findings establish that water is a byproduct of SW space weathering. We conclude, on the basis of the pervasiveness of the SW and silicate materials, that the production of radiolytic SW water on airless bodies is a ubiquitous process throughout the solar system.

solar wind radiolysis | prebiotic water | cosmic dust | astrobiology | aberration-corrected scanning transmission electron microscopy

There are two principal space weathering processes, solar wind (SW) ion irradiation and micrometeorite impacts, that produce rims on exposed mineral surfaces (1). Our focus here is on SW irradiation because of its possible connection to the production of water and hydroxyl radicals (2–5). Space-weathered rim thicknesses vary with the densities of implanted solar flare (SF) tracks, and track densities depend on the exposure ages of individual interplanetary dust particles (IDPs) in space. On lunar soil grains and grains on surfaces of IDPs, rims are typically 75–150 nm thick with SF track densities of 10^{10}–10^{11} cm^{-2} that are consistent with 10^4- to 10^5-y SW exposure ages (6, 7) (Fig. 1 *B–D*). Rims on asteroid Itokawa regolith grains are 30–60 nm thick with SF track densities of 5×10^9 cm^{-2} that are consistent with ~10^3-y exposure ages (8) (*Origins and Properties of Rims on IDPs, Asteroid Itokawa, and Lunar Soil Grains*). This correlation between amorphous rim thicknesses and SF track densities indicates that SW irradiation is the primary mechanism for amorphous rim formation. We examine rims on surface grains in IDPs because they are solely due to SW irradiation, whereas rims on lunar soil grains are due to SW irradiation, impact vapor deposition, or a combination of both (9), and remote observations suggest that if water is indeed produced in rims on lunar soil grains, it is not efficiently retained (10). Typical 5- to 25-μm diameter chondritic porous (CP) IDPs are low-density aggregates of predominantly submicrometer-sized grains, and they are collected in the stratosphere (11) (Fig. 1 *A–D* and *Origins of CP IDPs*). Chemical analyses of the rims on silicate grains at the surfaces of IDPs reveal that SW sputtering breaks atomic bonds and selectively removes cations (e.g., Mg), leaving a stoichiometric excess of oxygen and rendering the rims chemically reactive. Similar cation depletions and oxygen excesses are observed in amorphous rims produced during laboratory irradiation of crystalline silicate standards using H^+ and He^+ ions at SW fluences (12).*

Previous attempts to detect water in rims on the surfaces of irradiated oxygen-rich minerals using bulk analytical methods, where water, if present, is close to detection limits, have yielded conflicting results (13, 14). We used valence electron energy-loss spectroscopy (VEELS) because its ability to detect water in situ at the nanoscale has been demonstrated in aqueous liquids, biomaterials, and ices (15–17). VEELS characterizes the low-loss region of the energy loss spectrum (0–50 eV), where features due to plasmons, valence band transitions, −OH, and H_2O can be observed (12, 15–19). We detect water in the SW amorphous rims on nominally anhydrous CP IDPs. To confirm this identification and to evaluate the VEEL spectra water features as a function of local solid-state environment and incident electron dose, we compare our results from the IDPs with three sets of standards: man-made liquid cells, empty and water-filled (20); talc, a hydrous mineral [$Mg_3Si_4O_{10}(OH)_2$]; and H^+- and He^+-irradiated anhydrous silicates (a description of the liquid cell is provided in *Materials and Methods*).

Results

VEEL spectra from the empty and water-filled liquid cells and talc are compared in Fig. 2 *A–C*. The spectrum from the empty cell contains a single feature peaked at 23 eV, the volume plasmon,

Significance

Whether water is produced by solar wind (SW) radiolysis has been debated for more than four decades. In this paper, we exploit the high spatial resolution of electron microscopy and sensitivity of valence electron energy-loss spectroscopy to detect water (liquid or vapor) in vesicles within (SW-produced) space-weathered rims on interplanetary dust particle (IDP) surfaces. Water in the rims has implications for the origin of water on airless bodies like the Moon and asteroids, the delivery of water to the surfaces of terrestrial planets, and the production of water in other astrophysical environments. In particular, water and organic carbon were likely delivered simultaneously by the high flux of IDPs accreted by the early Earth and other terrestrial planets.

Author contributions: J.P.B., M.H.N., H.A.B., and M.C.M. performed research; H.A.I., J.J.G.-D., J.C., H.A.B., and M.C.M. analyzed data; and J.P.B., H.A.I., J.J.G.-D., J.C., and M.H.N. wrote the paper.

The authors declare no conflict of interest.

This article is a PNAS Direct Submission.

[1]To whom correspondence should be addressed. E-mail: johnbrad@hawaii.edu.

This article contains supporting information online at www.pnas.org/lookup/suppl/doi:10.1073/pnas.1320115111/-/DCSupplemental.

*Topanni A, Dukes C, Baragiola R, Bradley JP (2006) 37th Lunar Planet Sci Conf, March 13–17, 2006, League City, TX, abstr. 2056.

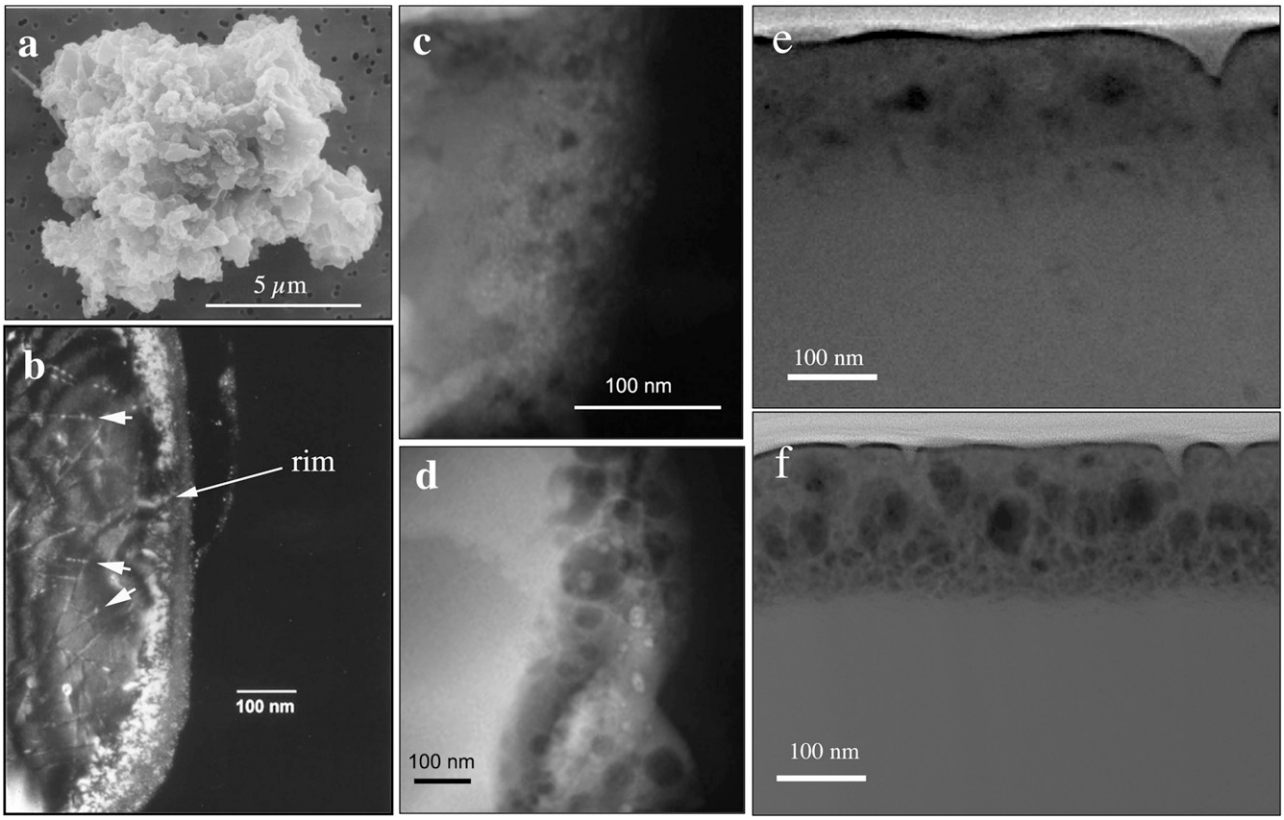

Fig. 1. (*A*) Secondary electron image of CP IDP U220A19. (*B*) Dark-field image of a pyroxene crystal on the surface of U220A19 with an ~100-nm thick amorphous rim resulting from SW irradiation. The linear features (arrows) in the pyroxene crystal are SF tracks. (*C*) High-angle annular dark-field (HAADF) density contrast image of the SW rim on the pyroxene showing vesicles within the amorphous silicate rim. (*D*) HAADF image of a vesiculated rim on a lunar soil anorthite crystal. Water was not detected in the vesicles. HAADF images of the amorphous rims on the surfaces of olivine (*E*) and anorthite (*F*) crystals following exposure to 5-keV He^+ (7.5×10^{18} He^+ per square centimeter) and 5-keV H^+ (1.0×10^{19} H^+ per square centimeter), respectively.

that is directly related to the specimen dielectric function (18). With water in the cell, a feature appears at 8.5 eV, and a second feature at 13.5 eV with fine structure extending to ~16 eV is sometimes observed. Depending on specimen thickness, a much weaker and broader third feature at 4.3 eV is observed. The 4.3-eV feature corresponds to the ionization threshold (IT) of water, the 8.5-eV feature corresponds to the energy gap (EG) of water, and the 13.5-eV feature is the hydrogen (H-K) core scattering edge (15–17, 21, 22).

Talc is thermally sensitive like other hydrated layer-lattice silicates that contain structurally bound water, and it decomposes in the electron beam to form enstatite ($MgSiO_3$), silica (SiO_2), and unbound water (H_2O) (23). Using VEELS, we monitored unbound water accumulation as a function of electron dose (Fig. 2 *D–F*). At low beam currents (0.05 nA), no water features are evident, but as the current is increased, both the IT and H-K edge features appear in conjunction with visible bubbling (rapid vesicle growth). A similar dependence of water features on electron dose and bubbling is observed when water ice is melted in the electron beam (16, 17).

The laboratory-irradiated anhydrous silicate mineral standards are olivine ($[Mg,Fe]_2SiO_4$), clinopyroxene ($[Ca,Mg,Fe]SiO_3$), and anorthite ($CaAl_2Si_2O_8$) (*Materials and Methods* and *SI Materials and Methods*). Both H^+- and He^+-irradiated standards have ~100-nm thick amorphous rims on their surfaces that contain vesicles 10–50 nm in diameter (Fig. 1 *E* and *F*). VEEL spectra from the rims differ from those from underlying mineral substrates (Fig. 2 *G–J*). The substrate spectra have relatively narrow volume plasmon peaks, typical of crystalline silicates, with weak surface plasmons between 8 eV and 12 eV originating from the upper and lower surfaces of the thin specimen. The volume plasmon peaks from the rims are significantly broader and are often shifted to a lower energy because surface plasmon contributions are greater due to irradiation-induced atomic-bond disruption, the presence of vesicles, and nanoporosity (12, 18, 19). Water IT, EG, and H-K features are observed in some vesicles in H^+-irradiated rims but not in He^+-irradiated rims, where, instead, the He-K core scattering edge at ~22 eV is observed in some vesicles (Fig. 2 *G–J*). A higher abundance of water-bearing vesicles was noted in the irradiated anorthite standard relative to the pyroxene and olivine standards.

VEEL spectra water features are similarly detected in amorphous rims and in vesicles contained within the rims on silicate grains in several CP IDPs (*Materials and Methods* and *SI Materials and Methods*). Fig. 3 *A–C* shows successive spectra from a vesicle at the base of the rim on a pyroxene crystal in CP IDP U220A19. Water IT, EG, and H-K features remain prominent until the electron beam perforates the vesicle, and they abruptly disappear as water escapes to vacuum. Spectra from the rim exhibit IT and EG features, and the pyroxene crystal exhibits only weak surface plasmons (Fig. 3 *D* and *E*). Relative to the spectrum from the pyroxene crystal, the rim spectra have a significantly broader plasmon peak shifted downward in energy by ~2 eV. A vesicle in the rim on another IDP (U2001 D7) exhibits IT, EG, and double-peaked H-K features, and the amorphous rim alongside the vesicle exhibits an IT feature (Fig. 3 *F* and *G*). We estimated the abundance of water in rims by X-ray energy dispersion spectroscopy (EDS) quantification of elemental abundances. Some SW rims on IDPs have up to 12 atomic percent excess O relative to oxide stoichiometry, attributable to, at most, ~1 weight percent water in the rims (*SI Materials and Methods*).

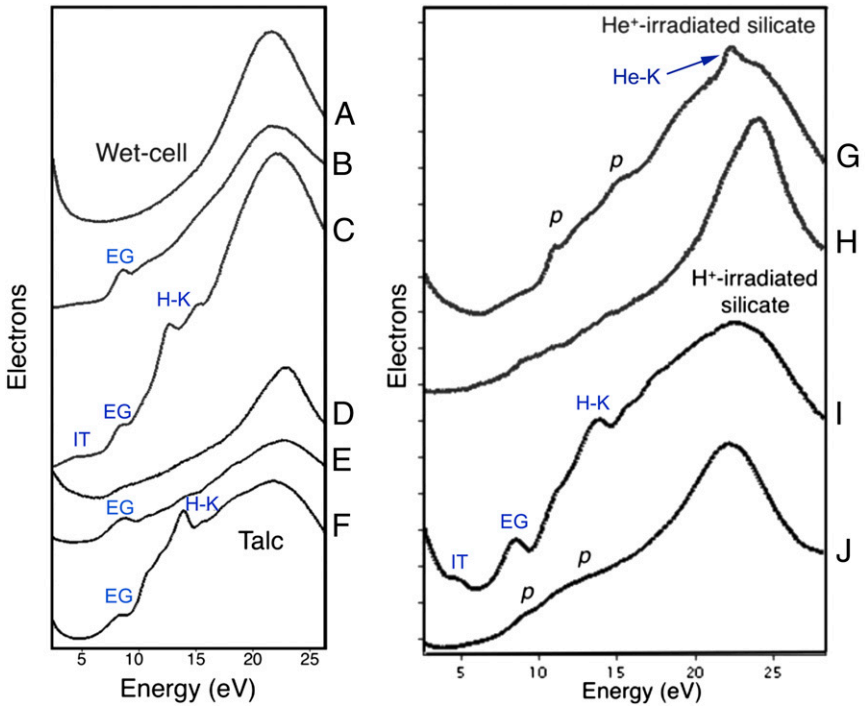

Fig. 2. VEEL spectra from an empty liquid cell (*A*) and two different locations in the water-filled cell (*B* and *C*). VEEL spectra from talc acquired over a constant time interval using a beam current of 0.05 nA (*D*), 0.15 nA (*E*), and 0.25 nA (*F*) are shown. (*G* and *H*) VEEL spectra from He^+-irradiated rim and olivine substrate. (*I* and *J*) Spectra from H^+-irradiated rim and anorthite substrate. IT, water IT; H-K, H-K core edge; *p*, surface plasmons. The beam current is ~0.05 nA for *G*–*I*. Details of mineral irradiation by He^+ and H^+ are provided in *SI Materials and Methods*.

Discussion

We find that detection of structurally unbound water in minerals using VEELS depends on the local physical environment of the water and incident electron dose. In a liquid cell, where water is not laterally confined, the position of the EG feature varies from 8 to 9 eV and the H-K feature may or may not be observed (15) (Fig. 2 *A*–*C*). With talc, the appearance of these features depends on electron dose and bubble formation, similar to water ice (Fig. 2 *D*–*F*). With water sealed in vesicles in SW rims, IT, EG, and H-K features are often immediately apparent even at low electron doses (e.g., Fig. 3 *A* and *B*). Prior studies of the VEEL spectra from liquid water and their degradation byproducts are sparse: Water dissociates in the electron beam, forming transient species that include H^+, $O^\bullet$, $OH^\bullet$, $H^\bullet$, H_2, H_2O_2, and $HO_2^\bullet$ (15–17). VEELS of molecular oxygen and hydrogen, which exhibit features at 13 eV and 15 eV, respectively, show that these peak positions are perturbed by formation of other stable molecules (e.g., CO, CO_2), which leads to an increase in the binding energy due to charge screening of the positive oxygen core (24). We attribute variations in the VEEL spectra water features to similar effects because, in addition to water, the rims and vesicles almost certainly contain Si-OH and possibly other species (e.g., carbon compounds) that were recoil-implanted into the rims by the SW.

Our detection of SW-produced water in rims on silicate mineral grains in nominally anhydrous IDPs has implications for production of water on the surfaces of airless bodies, its delivery to the surface of the Earth and other terrestrial planets, and production of water in the interstellar medium (3–5, 13).[†] For example, there is intense interest in water at the poles of the Moon (10, 25–27). A fundamental and as-yet unresolved question is the source of the water. Three sources have been proposed (*i*) primordial water present when the Moon formed and now sequestered in the lunar regolith, (*ii*) impacts by ice-rich comets and wet asteroids, and (*iii*) in situ water formation on the surfaces of oxygen-rich lunar mineral grains exposed to SW H^+ (1–3, 10, 25, 26). The sample analyses presented here, together with remotely sensed observations (10, 26), yield supporting evidence for the in situ creation of OH/H_2O by SW radiolysis of the lunar regolith. Previous sample studies have described the mechanism by which the SW could produce hydroxyl in the lunar regolith (5, 25). This study establishes that the SW does produce water in rims on silicate minerals. Although the VEELS data presented here are from CP IDPs, silicates and SW are common to both the Moon and asteroids. Hence, we infer that a similar process of creation of water must be occurring on these airless bodies, consistent with both our experimental findings and the lunar remote-sensing data. For example, anorthite is the most oxygen-rich of the silicates we examined, and we observed the highest abundance of vesicles with detectable water in the H^+-irradiated rim on the anorthite standard. The Moon-mineralogy imaging spectrometer detected the strongest hydroxyl absorption features associated with fresh craters in the anorthite-rich lunar highlands (26).

Although the remote observational data and our IDP sample analysis provide compelling evidence that the SW produces lunar water, detecting it in rims on lunar grains is expected to be challenging. Apart from at least two processes implicated in lunar rim formation (9), remote spectral data from the National Aeronautics and Space Administration's EPOXI mission (10) reveal a dynamic diurnal process of hydration, dehydration, and rehydration of the lunar regolith as a function of surface temperature that exceeds 100 °C in midlatitude regions. Typical CP IDPs, on the other hand, are from small frozen (cometary) parent bodies, and they can remain cold (≤10 °C) during their 10^4- to 10^5-y exposures to the SW while in solar orbit. They are pulse-heated for several seconds during entry, but the survival of

[†]Daulton TL, Bernatowicz TJ, Croat TK (2012) 43rd Lunar Planet Sci Conf, March 19–23, 2012, The Woodlands, TX, abstr. 2247.

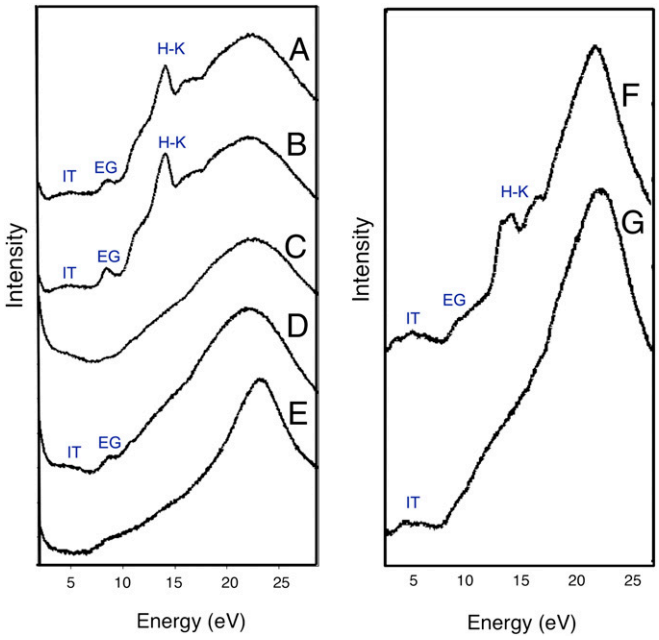

Fig. 3. VEEL spectra from an SW rim on a pyroxene ($Mg_{0.7}Fe_{0.3}SiO_3$) in CP IDP U220A19 using a defocused and monochromated beam with a 0.05-nA current. (*A* and *B*) Spectra obtained sequentially from a vesicle in the rim. (*C*) Spectrum from the vesicle following perforation by the electron beam. (*D*) Spectrum from the amorphous silicate rim on the pyroxene. (*E*) Spectrum from the underlying pyroxene crystal substrate. (*F*) Spectra from a vesicle in a rim on a pyroxene crystal. (*G*) Amorphous rim alongside the vesicle in CP IDP U2001 D7. Beam currents used were 0.05–0.1 nA.

SF tracks, near-saturation levels of implanted solar noble gases (He, Ne, and Ar), and volatile organic compounds show that low-density, highly porous CP IDPs can enter the atmosphere with minimal heating (11, 28–30) (Fig. 1*B*).

Water in rims on the surfaces of IDPs has implications for the delivery of water to the surfaces of terrestrial planets. The CP subset of IDPs studied here is part of the population of micrometeorites from comets and asteroids that continuously enter the Earth's atmosphere (*Origins of CP IDPs*). The present-day flux (30,000–40,000 tons/y) is comparable to, and possibly greater than, that of centimeter-to-kilometer size meteoritic objects from asteroids and comets; the flux may have been much higher on the early Earth (30, 31). Thus, some CP IDPs contribute both water and organic carbon simultaneously to the surface of the Earth and the other terrestrial planets.

Materials and Methods

We examined amorphous rims on the surfaces of H^+- and He^+-irradiated anhydrous silicate mineral standards and compared them with amorphous rims on anhydrous CP IDPs using an 80- to 300-keV aberration-corrected scanning transmission electron microscope equipped with a monochromator and high-resolution electron energy-loss spectrometer (*SI Materials and Methods*). IDPs were prepared by thin sectioning using ultramicrotomy (7) and by direct dispersion of disaggregated grains onto thin carbon films. The surfaces of polished thick-flat specimens of the mineral standards were irradiated using 5-keV H^+ and He^+ ions at fluences duplicating typical SW exposure ages (*SI Materials and Methods*). Electron-transparent cross-sections were harvested from the irradiated silicates and an unirradiated hydrated silicate standard, talc, using a focused ion beam instrument. The talc standard was decomposed in the electron beam to generate water as a first water standard. A second water standard was prepared using a wet cell that consists of a pair of electron-transparent silicon nitride windows, each ~100 nm thick, with a thin film of water sealed between them (20). The microstructures of the rims were examined using bright-field and dark-field imaging, and their elemental compositions were measured using EDS (*SI Materials and Methods*).

ACKNOWLEDGMENTS. This work was funded by the National Aeronautics and Space Administration's Cosmochemistry and Laboratory Analysis of Returned Samples (LARS) programs. Portions of this work were performed at Lawrence Livermore National Laboratory under the auspices of the US Department of Energy under Contract DE-AC52-07NA27344 and at the National Center for Electron Microscopy and Advanced Light Source Division, which are supported by the Office of Science, Office of Basic Energy Sciences of the US Department of Energy under Contract DE-AC02-05CH11231.

1. Hapke B (2001) Space weathering from Mercury to the asteroid belt. *J Geophys Res* 106(E5):10039–10073.
2. Liu YY, et al. (2012) Direct measurement of hydroxyl in the lunar regolith and the origin of lunar surface water. *Nat Geosci* 5:779–782.
3. Ichimura AS, Zent AP, Quinn RC, Sanchez MR, Taylor LA (2012) Hydroxyl (OH) production on airless planetary bodies: Evidence from H^+/D^+ ion-beam experiments. *Earth Planet Sci Lett* 345:90–94.
4. Greenwood JP, et al. (2011) Hydrogen isotope ratios in lunar rocks indicate delivery of cometary water to the Moon. *Nat Geosci* 4:79–82.
5. Lucey P, et al. (2006) Understanding the lunar surface and space-moon interactions. *Reviews in Mineralogy and Geochemistry* 60(1):83–219.
6. Bradley JP, Brownlee DE, Fraundorf P (1984) Discovery of nuclear tracks in interplanetary dust. *Science* 226(4681):1432–1434.
7. Bradley JP, Brownlee DE (1986) Cometary particles: Thin sectioning and electron beam analysis. *Science* 231(4745):1542–1544.
8. Noguchi T, et al. (2011) Incipient space weathering observed on the surface of Itokawa dust particles. *Science* 333(6046):1121–1125.
9. Noble S, Keller LP, Peiters CM (2005) Evidence of space weathering in regolith breccias I: Lunar regolith breccias. *Meteorit Planet Sci* 40(3):397–408.
10. Sunshine JM, et al. (2009) Temporal and spatial variability of lunar hydration as observed by the Deep Impact spacecraft. *Science* 326(5952):565–568.
11. Bradley JP (2013) Early solar nebula grains—Interplanetary dust particles. *Meteorites and Cosmochemical Processes*, Treatise on Geochemistry, ed Holland HD, Turekian KK (Elsevier–Pergamon, Oxford), 2nd Ed, Vol 1, pp 287–308.
12. Bradley JP, Dai ZR (2009) An analytical SuperSTEM for extraterrestrial materials research. *Meteorit Planet Sci* 44(10):1627–1642.
13. Djouadi Z, et al. (2011) Hydroxyl radical production and storage in analogues of amorphous interstellar silicates: A possible "wet" accretion phase for inner telluric planets. *Astron Astrophys* 531:A96–A104.
14. Burke DJ, et al. (2011) Solar wind contribution to surficial lunar water: Laboratory investigations. *Icarus* 211(2):1082–1088.
15. Jungjohann KL, Evans JE, Aguiar JA, Arslan I, Browning ND (2012) Atomic-scale imaging and spectroscopy for in situ liquid scanning transmission electron microscopy. *Microsc Microanal* 18(3):621–627.
16. Leapman RD, Sun S (1995) Cryo-electron energy loss spectroscopy: Observations on vitrified hydrated specimens and radiation damage. *Ultramicroscopy* 59(1-4):71–79.
17. Aronova MA, Sousa AA, Leapman RD (2011) EELS characterization of radiolytic products in frozen samples. *Micron* 42(3):252–256.
18. Yin NYS, Wang ZL (1999) Plasmon energy shift in mesoporous and double length-scale ordered nanoporous silica. *Appl Phys Lett* 74(18):2629–2631.
19. Hojou TK, Furuno S, Kuchita KN, Sasajima N, Izui K (1998) EELS analysis of SiC crystals under hydrogen and helium dual-ion beam irradiation. *Nucl Instrum Methods Phys Res B* 141(1-4):148–153.
20. Nielsen MH, et al. (2012) Structural evolution, formation pathways and energetic controls during template-directed nucleation of $CaCO_3$. *Faraday Discuss* 159:105–121.
21. Grand D, Bernas A, Amouyal E (1979) Photoionization of aqueous indole: Conduction band edge and energy gap in liquid water. *Chem Phys* 44(1):73–79.
22. Farhataziz H, Rodgers MAJ, eds (1987) *Radiation Chemistry—Principles and Applications* (VCH, New York).
23. De Souza H, Yada K (1988) Thermal transformation of talc as studied by electron-optical methods. *Clays Clay Miner* 36:289–297.
24. Crozier PA, Chenna S (2011) In situ analysis of gas composition by electron energy-loss spectroscopy for environmental transmission electron microscopy. *Ultramicroscopy* 111(3):177–185.
25. Hibbitts CB, et al. (2011) Thermal stability of water and hydroxyl on the surface of the Moon from temperature-programmed desorption measurements of lunar analog materials. *Icarus* 213(1):64–72.
26. Pieters CM, et al. (2009) Character and spatial distribution of OH/H2O on the surface of the Moon seen by M3 on Chandrayaan-1. *Science* 326(5952):568–572.
27. Greenwood JP, et al. (2011) Hydrogen isotope ratios in lunar rocks indicate delivery of cometary water to the Moon. *Nat Geosci* 4:79–82.
28. Brownlee DE (1985) Cosmic dust—Collection and research. *Annual Review of Earth and Planetary Sciences* 13:147–173.
29. Matrajt G, Messenger S, Brownlee DE, Joswaik DJ (2012) Diverse forms of primordial organic matter identified in interplanetary dust particles. *Meteorit Planet Sci* 47(4):529–549.
30. Love SG, Brownlee DE (1993) A direct measurement of the terrestrial mass accretion rate of cosmic dust. *Science* 262(5133):550–553.
31. Nesvorny D, et al. (2010) Cometary origin of the zodiacal cloud and carbonaceous micrometeorites. Implications for hot debris disks. *Astrophys J* 713(2):816–836.

Supporting Information

Bradley et al. 10.1073/pnas.1320115111

SI Materials and Methods

Specimen Preparation. Two sets of polished thick-flat specimens of the anhydrous silicate minerals anorthite ($CaAl_2Si_2O_8$), olivine ($[Mg,Fe]_2SiO_4$), enstatite ($[Mg,Fe]SiO_3$), and diopside ($[Ca,Mg]Si_2O_6$) were prepared. One set was irradiated with 5-keV He^+ at a fluence of ~7.5×10^{18} He^+ per square centimeter, and the other was irradiated with 5-keV H^+ at a fluence of ~1.0×10^{19} H^+ per square centimeter at the Laboratory for Atomic and Surface Physics at the University of Virginia.* Although the solar wind (SW) spectrum has a peak proton flux near 1 keV, 5-keV ions were used for the irradiation of the silicate mineral specimens to generate an H^+ depth penetration and rim with thicknesses comparable to those on interplanetary dust particles (IDPs). We note that He^+ and higher energy H^+, although much lower in abundance in the SW, cause significant damage at greater depths than the 1-keV H^+ comprising the majority of SW ions. These lower abundance ions result in a reduction of silicate density in the amorphized regions that allows further penetration of 1-keV H^+. Because the irradiated silicate mineral standards serve only to demonstrate whether unbound water forms under irradiation by each ion species, the incident ion energy is not critical. Because irradiated surfaces are susceptible to atmospheric moisture uptake, all prepared samples were continuously stored in either dry nitrogen or a low-humidity dry-box. The irradiated surfaces were sealed with a carbon coating, followed by a platinum coating deposited using a Nova NanoLab600 (FEI Co.) dual-beam focused beam (FIB) instrument equipped with an upgraded Sidewinder ion column (FEI Co.) and Ascend Xtreme Access (Ascend Instruments, LLC) and Autoprobe micromanipulators (Omniprobe, Inc.) at Lawrence Livermore National Laboratory (1, 2). The FIB instrument was also used to harvest electron-transparent cross-sections of the irradiated surfaces of the anhydrous silicates, as well as a section of the hydrated silicate mineral talc. Multiple chondritic porous (CP) IDPs were prepared using two different methods. U220A19 and U2001 D7, were embedded in low-viscosity epoxy (Embed 812; Electron Microscopy Sciences), followed by thin sectioning using an ultramicrotome equipped with a diamond knife (3). The sections were transferred to ultrathin carbon film substrates (10–20 nm thick) on transmission electron microscopy (TEM) mesh grids. A third CP IDP was gently disaggregated between quartz slides into its constituent grains, which were then mounted on a carbon-film TEM grid.

Electron Microscopy. We used an 80- to 300-keV Titan high-base scanning transmission electron microscope (FEI Co.) equipped with a monochromator, dual spherical aberration correctors, a Genesis 4000 Si(Li) solid-state X-ray energy-dispersive spectrometer (EDAX), and a Tridiem Imaging Filter/electron energy-loss spectrometer (Gatan) (4, 5). Conventional bright-field and dark-field TEM diffraction contrast (e.g., Fig. 1*B*) and high-angle annular dark-field (HAADF) scanning transmission electron microscopy (STEM) density-contrast imaging were used. HAADF images are especially useful for detecting vesicles in the rims that are otherwise invisible in conventional dark-field images (e.g., Fig. 1). Images were acquired at magnifications of 10,000× to 100,000×. The abundances of O, Mg, Al, Si, Ca, and Fe were measured quantitatively using X-ray energy dispersion spectroscopy (EDS) in conjunction with a Cliff–Lorimer thin-film correction procedure and thin-film standards (National Institute of Standards and Technology SRM2063 and ultramicrotomed mineral standards of enstatite, forsterite, and anorthite). For most measurements, relative error, determined chiefly by counting statistics and peak fitting, is <5% for O, Mg, Al, Si, Ca, and Fe.

We exploited two key advantages of the Titan high-base scanning transmission electron microscope: aberration correction that improves spectroscopic [EDS and valence electron energy-loss spectroscopy (VEELS)] signal to noise using low-beam currents (4–6) and VEELS, which enables detection of water that is highly localized at the nanometer scale and otherwise difficult to detect using bulk analytical techniques like IR spectroscopy, except in specimens with ideal geometries (7). VEELS was performed at 300 keV, with and without the monochromator, using an incident electron probe nominally at 1–2 Å (at focus) and a zero-loss peak energy resolution (FWHM) of 0.2–0.6 eV (*in vaccuo*), with acquisition times between 1 s and 30 s. VEELS was performed in scanning transmission mode (image coupling) using a dispersion of 0.03 eV per channel. The spectrometer collection angle was 6.6 mrad, and the convergence angle of the electron probe was 15 mrad. Hydrated silicates like talc (Fig. 2 *D–F*) are sensitive to relatively low electron beam currents, and anhydrous silicates, including olivine, pyroxene, and anorthite, can be sensitive to high electron beam currents. We systematically evaluated the stability of each specimen as a function of beam current to establish the threshold dose and time scale for the onset of radiation damage.

Due to the dynamic variation in spectral background, water content is not quantifiable by VEELS. To assess approximate levels of water in amorphous rims in IDPs, we instead used EDS: O was assigned in stoichiometric proportions to the detected cations (i.e., MgO, Al_2O_3, SiO_2, etc.), with the exception of $H^{(+)}$ because it is not detectable using EDS. In SW rims, "excess" O is primarily a consequence of SW irradiation that has resulted in preferential removal of cations like Mg and Ca via SW-induced element fractionation, leaving nonbridging O defects (1, 8). Excess O is assigned as $H^{(+)}{}_2O$. Due to uncertainties as to whether all local excess O has reacted to form unbound water, low incident electron beam currents and correspondingly low EDS signal from small volumes of vesicles, and high background from the high O content of surrounding amorphous silicate matrix, we calculate an upper limit only. Assuming minimal terrestrial contamination, SW rims of some CP IDPs contain, at most, 1 weight percent water, locally concentrated in sealed vesicles.

Origins of CP IDPs

Observations of meteors have shown that a significant fraction of the dust entering the Earth's atmosphere is from comets, and studies of the atmospheric fragmentation of cometary meteors show that they are composed predominantly of porous, extremely fragile objects (9). CP IDPs, aggregates of mostly submicron- to nanometer-sized component grains and organic carbon, are the most porous and fragile meteoritic objects known, and their anhydrous mineralogy and lack of evidence of postaccretional alteration are consistent with derivation from small, cold bodies without liquid water, such as comets and some asteroids (4, 10). The high speeds at which some of them enter the atmosphere are consistent with capture from cometary orbits,† and they have recently been collected from dust streams associated with specific comets (e.g., Grigg–Skjellerup).‡

*Topanni A, Dukes C, Baragiola R, Bradley JP (2006) 37th Lunar Planet Sci Conf, March 13–17, 2006, League City, TX, abstr. 2056.

†Brownlee DE, et al. (1995) 26th Lunar Planet Sci Conf, March 13–17, 1995, Houston, TX, abstr. 2247.

‡Nguyen AN, Busemann H, Nittler LR (2007) 38th Lunar Planet Sci Conf, March 12–16, 2007, League City, TX, abstr. 2332.

The silicate mineralogy and mid-IR spectral properties of CP IDPs are like those of the Comets Halley and Hale–Bopp and dissimilar to other classes of meteoritic materials (11–13). They are collected in the dry stratosphere at an altitude of ~20 km by impaction onto silicone oil-coated substrates or "flags" mounted on wing pylons on National Aeronautics and Space Administration WB57 aircraft (13). Typical 10- to 25-μm CP IDPs have the highest porosities and lowest densities of known meteoritic materials, resulting in gentle deceleration in the upper atmosphere and minimal frictional heating and intact space-weathered amorphous rims in many cases (14, 15).

Origins and Properties of Rims on IDPs, Asteroid Itokawa, and Lunar Soil Grains

The correlation between amorphous rim thickness and density of solar flare tracks in IDPs and asteroid Itokawa grains establishes that the rims are due solely to SW irradiation (4, 15–17). In addition, TEM and STEM imaging of ultramicrotomed thin sections of whole IDPs of sufficiently low density to avoid significant atmospheric entry heating allows confirmation that rims are present around the outer surfaces that were exposed directly to the SW. Whether any vesicles in rims on Itokawa grains contain detectable water has yet to be investigated. The densities, mineralogy, and compositions of SW rims often differ significantly from the underlying (nonirradiated) mineral substrates due to selective sputtering and recoil implantation of atoms from adjacent grains. For example, rims on the most common silicates in IDPs, Mg-Fe olivine and pyroxenes, can be depleted in Mg and contain nanometer-sized metallic Fe^0 crystals produced by in situ reduction of Fe^{2+} in the silicate to Fe^0 (16). SW rims on some Itokawa silicates contain both nanophase iron and iron sulfides (18). The origin of rims on lunar soil grains is less certain; in addition to SW irradiation, deposition of vapors from micrometeorite impacts is believed to contribute to the rims, and the relative contributions of these processes have long been debated (19–21).

1. Graham G, et al. (2008) Applied focused ion beam techniques for sample preparation of astromaterials for integrated nanoanalysis. *Meteorit Planet Sci* 43(3):561–569.
2. Ishii HA, et al. (2010) Discovery, mineral paragenesis, and origin of wadalite in a meteorite. *American Mineralogist* 95(4):440–448.
3. Bradley JP, Brownlee DE (1986) Cometary particles: Thin sectioning and electron beam analysis. *Science* 231(4745):1542–1544.
4. Erni R, Browning ND, Dai ZR, Bradley JP (2005) Analysis of extraterrestrial particles using monochromated electron energy-loss spectroscopy. *Micron* 36(4):369–379.
5. Bradley JP, Dai ZR (2009) An analytical SuperSTEM for extraterrestrial materials research. *Meteorit Planet Sci* 44(10):1627–1642.
6. Smith DJ (2008) Development of aberration-corrected electron microscopy. *Microsc Microanal* 14(1):2–15.
7. Djouadi Z, et al. (2011) Hydroxyl radical production and storage in analogues of amorphous interstellar silicates: A possible "wet" accretion phase for inner telluric planets. *Astron Astrophys* 531:A96–A104.
8. Pillinger CT (1979) Solar-wind exposure effects in the lunar soil. *Rep Prog Phys* 42(5): 897–961.
9. Verniani F (1969) Structure and fragmentation of meteoroids. *Space Sci Rev* 10(2):230–261.
10. Bradley JP (2014) Early grains in the solar nebula—Interplanetary dust particles. *Meteorites and Cosmochemical Processes,* Treatise on Geochemistry, ed Holland HD, Turekian KK (Elsevier–Pergamon, Oxford), 2nd Ed, Vol 1, pp 287–308.
11. Bradley JP (1988) Analysis of chondritic interplanetary dust thin sections. *Geochim Cosmochim Acta* 52(4):889–900.
12. Bradley JP, et al. (1999) An infrared spectral match between GEMS and interstellar grains. *Science* 285(5434):1716–1718.
13. Molster FJ, Waters LBFM (2003) *Astromineralogy*, ed Henning Th (Springer, New York), pp 121–170.
14. Brownlee DE (1985) Cosmic dust—Collection and research. *Annual Review of Earth and Planetary Sciences* 13:147–173.
15. Sandford SA, Bradley JP (1989) Interplanetary dust particles collected in the stratosphere: Observations of atmospheric heating and constraints on their interrelationships and sources. *Icarus* 82(1):146–166.
16. Bradley JP, Brownlee DE, Fraundorf P (1984) Discovery of nucler tracks in interplanetary dust. *Science* 226(4681):1432–1434.
17. Bradley JP (1994) Chemically anomalous, preaccretionally irradiated grains in interplanetary dust from comets. *Science* 265(5174):925–929.
18. Noguchi T, et al. (2011) Incipient space weathering observed on the surface of Itokawa dust particles. *Science* 333(6046):1121–1125.
19. Bernatowicz TJ, Nichols RH, Jr., Hohenberg CM, Maurette MM (1994) Vapor deposits in lunar regolith: Technical comment. *Science* 264(5166):1779–1780.
20. Lucey P, et al. (2006) Understanding the lunar surface and space-moon interactions. *Reviews in Mineralogy and Geochemistry* 60(1):83–219.
21. Liu Y, et al. (2012) Direct measurement of hydroxyl in the lunar regolith and the origin of lunar surface water. *Nat Geosci* 5:779–782.